HIGH SPATIAL RESOLUTION MID-INFRARED OBSERVATIONS OF THREE SEYFERT GALAXIES

B. T. Soifer,[1,2] J. J. Bock,[3,4] K. Marsh,[5] G. Neugebauer,[1,6] K. Matthews,[1] E. Egami,[1,6] and L. Armus[2]

ABSTRACT

Images at 12.5 μm of nuclei of three nearby Seyfert galaxies—NGC 1275, NGC 4151, and NGC 7469—have been obtained with the 10 m Keck Telescope. NGC 7469 is resolved and deconvolution delineates a structure ($<0\rlap{.}''04$) $\times 0\rlap{.}''08$, or less than 13×26 pc at a position angle of $135°$. From a comparison with structure seen at millimeter wavelengths, this structure is interpreted as a disk aligned with the molecular gas in the central few hundred parsecs of the galaxy. NGC 1275 and NGC 4151 are not resolved; limits on the sizes of these nuclei are $0\rlap{.}''08$ and $0\rlap{.}''16$, corresponding to physical spatial scales of 28 and 10 pc. The lower limits to the brightness temperatures implied by these size limits and the measured flux densities are within $\sim$50 K of the 12–25 μm color temperatures of these systems, as inferred from *IRAS* observations. The angular size limits are within a factor of 2 of the sizes required to spatially resolve thermal emission from dust heated by a central luminosity source. These sizes preclude significant contributions to the nuclear infrared emission from star-forming regions.

Key words: galaxies: individual (NGC 1275, NGC 4151, NGC 7469) — galaxies: Seyfert — infrared radiation

1. INTRODUCTION

There is much evidence (e.g., Krolik 1999) that nonthermal processes power the nuclei, i.e., the central sources, of Seyfert galaxies. In the mid-infrared, however, thermal radiation from heated dust contributes an additional emission component. This mid-infrared radiation, at characteristic temperatures of a few hundred kelvins, is believed to emerge from a disklike structure that is heated by the inner accretion disk (Sanders et al. 1989). A question remains of the geometry of the central, presumably mainly nonthermal, source and how much of the surrounding dust is heated by the central source and how much is heated by starbursts that are located throughout the nucleus and thus form an extended cloud. It is difficult to resolve this dust component in direct observations using currently available telescopes because the angular extent of the region containing the emitting dust is small. Quantitatively, the Seyfert galaxies considered here have observed luminosities of 10^{10}–10^{11} $L_\odot$. If the dust is at a temperature of $\sim$300 K—the temperature at which blackbody emission peaks at 12.5 μm—and is heated by a central source, it is predicted to have a separation from the central source 2–20 pc, or less than $0\rlap{.}''1$, depending on the composition of the dust. If, on the other hand, the dust were heated by hot stars in starburst regions, the extent of the region containing dust clouds could be much larger.

The diffraction-limited full width at half-maximum (FWHM) of the 10 m Keck Telescope—the largest aperture telescope currently available—is $0\rlap{.}''31$ at 12.5 μm. Deconvolution techniques and proper sampling of a nearby point-spread function (PSF) can improve this resolution significantly. For example, deconvolution applied to the image of NGC 1068—the nearest and brightest Seyfert galaxy—have successfully resolved structure with a size of $0\rlap{.}''1$ ($\sim$7 pc at the distance of NGC 1068; Bock et al. 2000).

In this paper, we present observations of the nuclei of three nearby, infrared bright Seyfert galaxies—NGC 1275, NGC 4151, and NGC 7469—taken with the 10 m Keck Telescope. These observations, when deconvolved, approach the angular resolution necessary to distinguish thermal from nonthermal emission and, in one case, resolve the structure of the central source. In the mid-infrared, all three galaxies are known to contain a strong pointlike nucleus, and the observations were designed, and optimized, to probe this source. As a result, they are not optimized to delineate low surface brightness, extended emission. They are thus complementary to observations such as those by Radomski et al. (2003) of NGC 4151. We take the Hubble constant to be 75 km s^{-1} Mpc^{-1}.

2. SAMPLE

The characteristics of the three Seyfert galaxies (Seyfert 1943), taken from the literature, are shown in Table 1. All are known to be bright in the mid-infrared (*IRAS* Point Source Catalog 1989; Miles et al. 1996). NGC 1275 and NGC 4151 are both compact in the mid-infrared. Miles et al. have shown, from observations at $\sim$10 μm with $0\rlap{.}''7$ resolution, that NGC 7469 consists of a compact nucleus surrounded by a lumpy ring $\sim$3″ in diameter. The ring is presumably a region of active star formation. Miles et al. found that the nucleus plus ring structure in NGC 7469 accounts for $\sim$60% of the total 12 μm flux density of the galaxy measured by *IRAS*.

3. OBSERVATIONS

The observations were made using the Keck Long Wavelength Spectrometer (LWS; Jones & Puetter 1993) in the

SOIFER ET AL.

TABLE 1
SAMPLE

OBJECT	SEYFERT TYPE	REDSHIFT	SCALE (pc arcsec^{-1})	IRAS f_ν (Jy) 12 μm	25 μm	log [$L_{IR}(L_\odot)$][a]
NGC 1275..............	2	0.0176[b]	350	1.17	3.50	11.24
NGC 4151..............	1.5	0.0033[c]	65	1.95	5.04	9.86
NGC 7469..............	1.2	0.0163[d]	326	1.60	5.40	11.59[e]

[a] Based on *IRAS* observations from 12 to 100 μm.
[b] From Strauss et al. 1992.
[c] From de Vaucouleurs et al. 1991.
[d] From Keel 1996.
[e] Luminosity of both nucleus and 3″ diameter ring.

imaging mode at 12.5 μm ($\Delta\lambda = 1.16$ μm) at the f/25 forward Cassegrain focus of the Keck I 10 m Telescope. The LWS Si:As array has 128×128 pixels. The scale is 0″08 pixel^{-1} giving a field of $\sim 10'' \times 10''$. A log of the observations is given in Table 2.

In the mid-infrared, there were no stars in the field from which to estimate point-source profiles. Each measurement of the object size was therefore accompanied by multiple observations of one of the three bright stars, identified as the PSF in Table 2, which was nearby to the object and of comparable infrared brightness. The observations were made in runs of 27–54 s by interleaving imaging of the galaxy with observations of the PSF star; the number of comparisons between the galaxy and the PSF star is also indicated in Table 2. The telescope was guided during the observations of the objects using a visual guider on stars near the galaxies.

For these observations, objects and PSF calibrators were imaged in a chop-nod scheme, where the throw of the secondary chopper was equal to the amplitude of the (telescope) nod. The amplitude of the secondary chopper was set to 5″–15″ at a frequency ~ 5 Hz.

All three nights were photometric, and in all cases the air mass was between 1.0 and 1.4. Each sequence to measure the object size was preceded by an observation of one of the three bright stars—α Tau = HR 1457, α Boo = HR 5340, or β Peg = HR 8775—in order to obtain a photometric calibration.

4. DATA REDUCTION AND ANALYSIS

4.1. *Photometry*

Photometric measurements were made from the raw images before any deconvolution algorithms (described below) were applied. The photometry of the galaxies was based on the following magnitudes (in the Vega based

system)—HR 1457, [12.5 μm] = -3.07 mag; HR 5340, [12.5 μm] = -3.15 mag; and HR 8775, [12.5 μm] = -2.55 mag. The "sky" was taken as an annulus 4″6–6″0 in diameter. The conversion from magnitude to flux density followed the prescription given in the Explanatory Supplement to the *IRAS* Catalog (Beichman et al. 1985); i.e., at 12.5 μm, 0.0 mag was taken as 26.15 Jy.

4.2. *General Image Data Reduction*

The images were processed following a similar procedure to that described in Bock et al. (2000), briefly summarized as follows. Images were obtained by shifting and combining subimages after every chop pair, using only the central image, to eliminate any possibility of nonreproducibility in the telescope nod, i.e., potential differences caused by guiding the telescope were obviated in software by finding the centroid of each object image in each nod. Both end chop images did not always fall onto the array, so were not used in the data reduction. The results when the end images were included, however, were found to be appreciably the same.

For the PSFs, which were not guided, each chop-nod combination consisted of four separate images, which were combined to produce three images: an image near the middle of the array and two images near the edge or off the array. The middle image was thus seen twice, first in the positive beam of the first chop pair, and then in the negative beam of the second chop pair. The objects were guided, and eight subimages were combined into the three images; the middle image was thus seen four times. The object and PSF calibrator images were subpixel shifted, rotated, and co-added using a routine that relies on sub-Nyquist sampling of the images. The objects were rotated from array coordinates to equatorial north coordinates during the combination. The PSF calibrators were rotated through a sequence of rotations in array coordinates matched to the object. The rotations were designed to best match the orientation of the

TABLE 2
LOG OF OBSERVATIONS

OBJECT	DATE (2000)	PSF STAR	INTEGRATION TIME[a] (s) Object	PSF	NUMBER OF PSF COMPARISONS
NGC 1275..............	Dec	IRC +40060	30	27	9
NGC 4151..............	May	HR 4550	54	54	2
NGC 7469..............	Sep	HR 8815	81	54	4

[a] Integration time in each comparison.

characteristic six-pointed diffraction pattern as it appeared on the array for both object and PSF calibrator. This pattern is fixed with respect to the telescope and thus in parallactic angle and therefore rotates in the field as the telescope tracks. The resulting PSF was thus not rotated to equatorial north, but was rotated through a superposition of rotation angles corresponding to the orientation of the diffraction pattern of the object sequence as it appeared on the array. The rotations for each PSF/object combination were always matched pairwise, producing a matched PSF for every subset of object images under consideration.

4.3. *FWHM Analysis*

Because the combined images of the objects were all very nearly pointlike and closely resembled the combined PSF calibrator images, and variations in the PSF, not statistical noise, dominated the overall uncertainty in deconvolving these images, it was necessary to evaluate the stability of the PSF by comparing the raw object and PSF calibrator images before proceeding to image deconvolution. An estimate of the intrinsic source size of the object was obtained by assuming the sizes add in quadrature

$$\theta_{\rm INT}^2 = \theta_{\rm OBJ}^2 - \theta_{\rm PSF}^2 \ ,$$

where $\theta_{\rm INT}$ is the intrinsic source size of the object, $\theta_{\rm PSF}$ is the observed PSF size, and $\theta_{\rm OBJ}$ is the observed object size all expressed as FWHM. An estimate of the uncertainty can be obtained from $\delta\theta_{\rm INT}^2$, the dispersion of $\theta_{\rm INT}^2$ in the population of pairs. We will take the quantity $\theta_{\rm UL} = [\langle\theta_{\rm INT}^2\rangle + \delta\theta_{\rm INT}^2]^{1/2}$ as the estimate of the upper limit on the source size. It should be noted that this definition takes account of the fact that the objects and PSFs are often comparable in size, and the fact that the size of the object image on occasion exceeds that of the PSF.

4.4. *Deconvolution*

Each combined object image was deconvolved by a matched PSF calibrator image using the Richardson-Lucy procedure (Richardson 1972; Lucy 1974) as encoded in the IDL maximum likelihood routine (Varosi & Landsman 1993). The images were interpolated to a 4 times finer pixel scale before deconvolution. The reconvolved image was rebinned and subtracted from the original image and compared with the estimated statistical uncertainty per pixel. It was found, however, that the uncertainties were largest where the image was brightest and were always greater than the statistical uncertainties even after iterating the deconvolution routine a large number of times. The nonuniform uncertainties from deconvolution must be compared to a combination of statistical and PSF uncertainties in the region of image of

interest. Therefore, we chose to stop iterating the deconvolution routine when the residuals were consistent with the measurement uncertainties in the raw images.

5. RESULTS

NGC 7469 showed a statistically significant detection of structure, while the images of NGC 1275 and NGC 4151, combining all the data, both showed a single pointlike compact nucleus. The FWHM of various angular quantities, obtained before deconvolution was applied, are given in Table 3. Although the uncertainties on the $\langle\theta_{\rm INT}^2\rangle^{1/2}$ are small, we claim, to be conservative, only to have measured a limiting size for the nuclei of NGC 1275 and NGC 4151 of $\theta_{\rm UL}$. It should be noted that the PSF during the NGC 7469 observations was noticeably more compact and significantly more stable than for any of the other objects. Deconvolution applied to the combined NGC 7469 image confirmed the presence of clear structure.

In the case of NGC 1275 and NGC 7469, the data were extensive enough to provide several sets of the object and the PSF calibrator. The images were paired to both match the object and PSF calibrator images in air mass and to minimize the time interval between the two images. Unfortunately, the NGC 4151 data were quite limited, resulting in only two image pairs. In order to obtain a meaningful limit, the data were simply subdivided into five image pairs. This is less than ideal, since the pairs all have a common time interval, and the matching in air mass was poor. Further subdividing the NGC 4151 images was possible but gave a nearly identical result. From the present data, we conclude that 0″.16 is an upper limit to the size of the nucleus. In comparison, Neugebauer et al. (1990), using slit scans and a single-element detector, determined the size of the nucleus of NGC 4151 at 11.2 μm to be 0″.16 ± 0″.04. The deconvolved images of NGC 4151 and NGC 1275 do not show structure, and these sources appear to be unresolved in these observations. As stated above, the deconvolution algorithm did not improve the size limit beyond that set by the variations in the PSF, and we choose to quote the upper limit of the sizes as the size estimated in the analysis of the FWHM in the raw images.

As expected from the work of Miles et al. (1996), the raw images of NGC 7469 show a bright compact nucleus surrounded by a fainter ring. The flux from the ring, which has a diameter of $\sim3''$ and is well separated from the nucleus, is comparable to that of the nucleus. The surface brightness from the ring is less than 5% of the brightness of the central source in the raw image. (Note that because of the small chop amplitude of these observations we cannot make a reliable flux measurement in an adequately large beam to determine this ratio.)

TABLE 3
FWHM ANALYSIS

Object	$\langle\theta_{\rm OBJ}\rangle$[a] (arcsec)	$\langle\theta_{\rm PSF}\rangle$[a] (arcsec)	$\langle\theta_{\rm INT}^2\rangle^{1/2}$[b] (arcsec)	$\theta_{\rm UL}$ (arcsec)
NGC 1275..............	0.35 ± 0.02	0.34 ± 0.02	$0.06^{+0.02}_{-0.03}$	0.08
NGC 4151..............	0.38 ± 0.02	0.36 ± 0.05	$0.10^{+0.06}_{-0.10}$	0.16
NGC 7469..............	0.276 ± 0.006	0.270 ± 0.003	0.070 ± 0.005	0.08

[a] Uncertainties are sample standard deviation of $\theta_{\rm OBJ}$ or $\theta_{\rm PSF}$.
[b] Uncertainties calculated from standard deviation in $\langle\theta_{\rm INT}^2\rangle$.

TABLE 4
RESULTS AND DERIVED QUANTITIES

OBJECT	f_ν (Jy) 12 μm[a]	f_ν (Jy) 12.5 μm	SIZE[b] 12.5 μm (arcsec)	SIZE[b] 12.5 μm (pc)	$T_{Brightness}$ 12.5 μm (deg)	T_{Color} 12/25 μm (deg)	DIAMETER $T_C = T_B$ (arcsec)	SURFACE BRIGHTNESS[c] ($10^{14} L_\odot$ kpc^{-2})
NGC 1275.............	1.17	1.00[d]	<0.08	<27	>150	192	0.04	>2.8
NGC 4151.............	1.95	2.31[d]	<0.16	<10	>139	201	0.04	>0.9
NGC 7469.............	1.60	0.65[e]	(<0.04) × 0.08	(<13) × 26	>148	185	0.03	>4.6[f]

[a] For the convenience of the reader, the flux densities obtained by *IRAS* at 12 μm are repeated here.
[b] Limits are θ_{UL}.
[c] A 12.5 μm surface area, infrared luminosity.
[d] A 4″ diameter beam, raw image, not deconvolved.
[e] A 1″4 diameter beam, raw image, not deconvolved.
[f] Big beam (*IRAS*) luminosity value times 0.4.

Photometric results are included in the summary of Table 4. With 20% uncertainties, the flux densities of the compact sources of NGC 1275 and NGC 4151 reported here at 12.5 μm agree with those measured at 12 μm by *IRAS* in a 4″5 × 0″8 beam. These results are consistent with the results on NGC 4151 reported by Radomski et al. (2003), who find that 73% of the 10 μm broadband flux is in an unresolved component. We will assume that the luminosity and color as measured by *IRAS* applies to the compact sources. The flux density of the compact nucleus of NGC 7469 inside a 1″4 diameter beam is 40% of the flux density at 12.0 μm measured in the much larger *IRAS* beam.

5.1. *Deconvolution of NGC 7469*

The deconvolved image of NGC 7469, after combining all the data, shows significant structure both in the ring and in the nucleus. The deconvolution routine reaches statistical noise on the 3″ diameter ring in about 10 iterations, due to

its low surface brightness. Maximum likelihood does not perform well on images like this requiring large dynamic range, and we note that although many more iterations are needed to resolve the nucleus, they are of no further use in resolving the ring. The deconvolution of the image with 10 iterations, thus emphasizing the 3″ diameter ring, is shown in Figure 1. For purposes of deconvolving the nucleus, the ring does not affect the images of the central source. This assertion was tested by deconvolving a 3″8 × 3″8 image of NGC 7469 containing the ring and by deconvolving a 1″6 × 1″6 image of NGC 7469 excluding the ring. Both deconvolutions produce essentially identical images of the inner 1″ × 1″ nucleus. In the following, we will often designate the central nucleus of NGC 7469 simply as " NGC 7469."

The deconvolved image of the NGC 7469 nucleus with 1000 iterations of the deconvolution algorithm is presented in Figure 2 and shows extended structure that is statistically significant based on the estimate of PSF variations. The
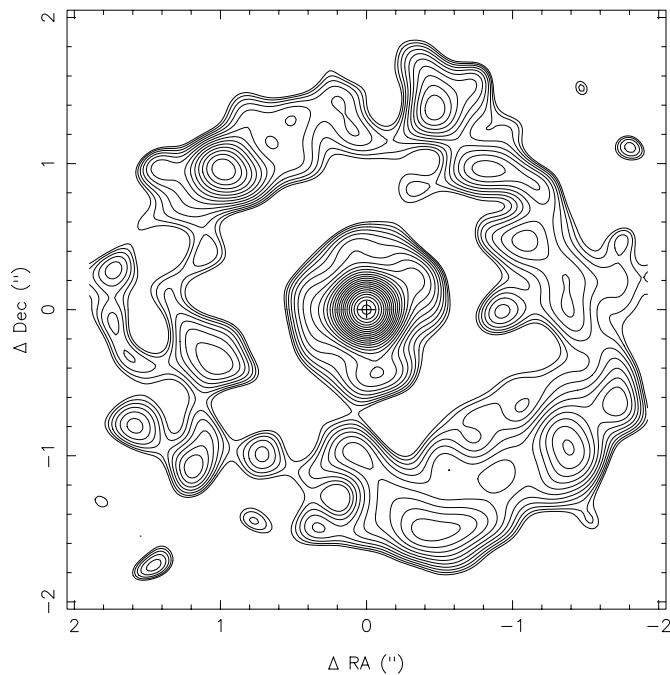

FIG. 1.—Deconvolved image of NGC 7469. There were only 10 iterations in the deconvolution, so the faint ring with ∼3″ diameter is emphasized. The image is displayed with contours spaced by multiplicative factors of 1.342, ranging from 90% of maximum, so that the third contour represents the 50% level. North is up, and east is to the left.
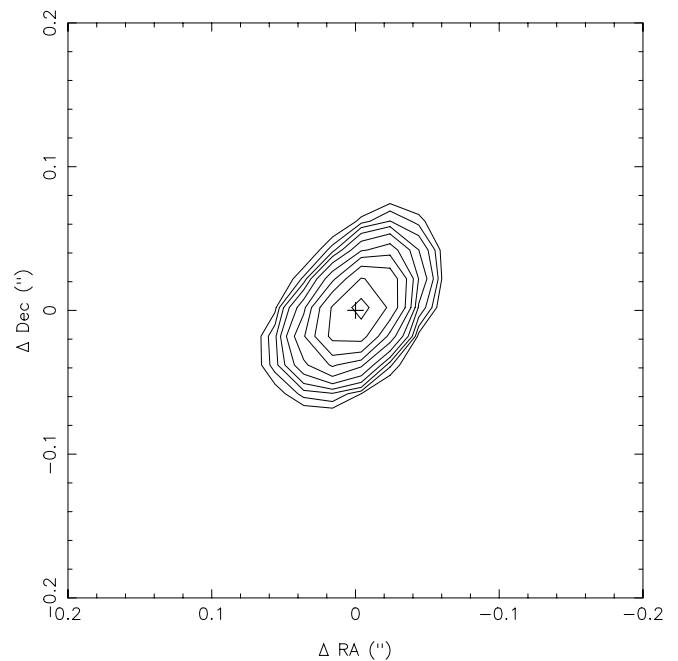

FIG. 2.—Deconvolved image of NGC 7469 shown with 1000 iterations in the deconvolution thus emphasizing the nucleus. The image is displayed with contours spaced by multiplicative factors of 1.342, ranging from 90% of maximum, so that the third contour represents the 50% level. North is up, and east is to the left.

robustness of the deconvolution technique was tested by subdividing the observations of the PSF into subgroups and treating successive subgroups as objects. This test is described in Appendix A. The reproducibility of the extension shown in Figure 2 was likewise tested by subdividing the data into independent object and PSF calibrator images and deconvolving the corresponding image pairs, as shown in the Appendix B. The statistical significance can be evaluated quantitatively by comparing the quality of fit of the hypothesized elongated source to that obtained under the assumption of a simple point source. This procedure is described in Appendix C with the result that the elongation is estimated to be significant at the $4.3\,\sigma$ confidence level.

To summarize the appendices, we conclude the extension of $(<0\rlap{.}''4) \times 0\rlap{.}''08$ seen in NGC 7469 is real for the following reasons:

1. The structure in NGC 7469 was detected statistically based on the FWHM of the object and the PSF.

2. The deconvolved PSF images, synthesized from the observations for matching in time and air mass, are point-like and more compact than the deconvolved images of NGC 7469.

3. The deconvolved images using independent pairs of NGC 7469 and the PSF produce consistent results with a northwest-southeast extension of similar size and direction.

5.2. *Extended Emission*

Although the observations were not optimized to study extended emission, the quantity and quality of the data on NGC 1275 and NGC 7469 were sufficiently great to attempt an examination of the extended emission using the technique exploited successfully by Radomski et al. (2003) in the study of NGC 4151. These high-resolution images, combined with a precise knowledge of the PSF, allow us to best probe extended emission close to the nucleus.

In Figure 3, two sets of differences—the galaxy minus the PSF and the galaxy minus a fraction of the PSF—are given. There is evidence in NGC 7469 for emission in the northwest-southeast direction—i.e., the orientation of the structure in the deconvolved image—extending almost $1''$, while in NGC 1275 there is an indication of extended emission in the north-south direction. The putative extended emission is only about 3 times brighter than the PSF residuals, so we advise caution in interpreting these images, especially at the radius of the first Airy maximum (radius $= 0\rlap{.}''4$). Although faint, the extended emission reproduces itself if the images are constructed using independent subsets of the data from the first half and second half of the observations, in spite of the fact that the change in parallactic angle rotates the apparent diffraction pattern by $10°$. In NGC 7469, the structure noted here is also seen in Figure 1.

6. DISCUSSION

The observations at $12.5\,\mu$m with the 10 m Keck Telescope yield a resolved structure in NGC 7469, but give only limits for the size of NGC 1275 and NGC 4151 (see Table 4). At the distances of the galaxies, the limits on the angular sizes correspond to linear size limits of 10 pc in NGC 4151 and 27 pc in NGC 1275. Although an asymmetry is obvious in NGC 1068 at a comparable physical scale, none is obvious in NGC 4151 in our images. The physical tempera-

tures implied for dust grains heated by a central source of luminosity are between 300 and 450 K depending on the sizes of the individual grains and their composition. This is substantially hotter than the observed color temperature, based on *IRAS* 12 and 25 μm data, of 192 and 201 K for NGC 1275 and NGC 4151, respectively. As shown in Table 4, the limits on the sizes in these sources are not small enough to require optically thick emission, but the lower bound on $\tau_{12.5\mu m}$ is 0.25 in NGC 1275 and 0.06 in NGC 4151 if the emission is thermal emission at the color temperature determined from the *IRAS* 12 μm to 25 μm flux density ratio. This calculation, of course, requires the reasonable assumption that the source structure is essentially the same at 25 and 12 μm.

In the case of NGC 7469, the resolved structure provides strong direct evidence for the dust thermal emission model in the nucleus, as well as a limit of $\tau_{12.5\mu m} > 0.4$ within this structure (Table 4). The elongated structure is suggestive of a disk geometry. The "standard model" of an active galactic nucleus (AGN; e.g., Krolik 1999; Sanders et al. 1989) suggests that this disk is heated by the central AGN. The fact, noted above, that graphite and silicate dust grains at distances of ~15 pc from the central source, i.e., at the linear radius corresponding to the angular size of the structure, are heated to temperatures of 300–450 K, well above the observed color temperature, is consistent with this picture. The derived brightness temperature, again well below 300 K, is only a limit since the source is unresolved in one dimension.

An interesting question is what the relationship of the infrared nucleus is to the nuclear structure of the galaxy observed in the radio. Observations by Thean et al. (2001) at 1.6 GHz (18 cm) at $\sim0\rlap{.}''3$ resolution show structure whose orientation is very similar to that seen in the mid-infrared structure. A similar feature is also seen at 4.9 GHz (6 cm) in the VLA image of Wilson et al. (1991). Although again at a much lower spatial resolution ($2''$) than that seen here in the mid-infrared, high-resolution maps in CO (Meixner et al. 1990) show emission, interpreted as a rotating molecular disk, whose orientation also is similar to that seen in the mid-infrared structure.

VLBI observations of Lonsdale et al. (2003) at 18 cm show that the nucleus of NGC 7469 is a nearly symmetric linear triple source aligned in the east-west direction with the outer components separated by $0\rlap{.}''15$, and the central source nearly centered between these two components. The agreement between the centroids of the radio peak, as described by Lonsdale et al., and the mid-infrared peaks is excellent, with the two peaks coinciding to within $0\rlap{.}''040$ if the $3''$ ring structures are assumed to be spatially coincident. The uncertainty in the determination of the astrometric coincidence of the radio and infrared nuclei is determined by how well the structures in the $3''$ ring can be aligned.

We have compared the mid-infrared image of Figure 2 with the VLBI image of Lonsdale et al. (2003) in Figure 4. The position angle of the elongated structure at 12.5 μm is $135°$, $\sim45°$ off of the position angle of the linear radio structure. To register the images in Figure 4, we assumed that the middle radio peak coincides with the AGN and is centered on the mid-infrared peak. Then the two outer radio components are symmetrically placed with respect to the mid-infrared disk and is suggestive of radio jets emerging out of the plane of the dust disk. If the galaxy is assumed to be circular, its apparent size on the sky—$1\rlap{.}'1 \times 1\rlap{.}'5$
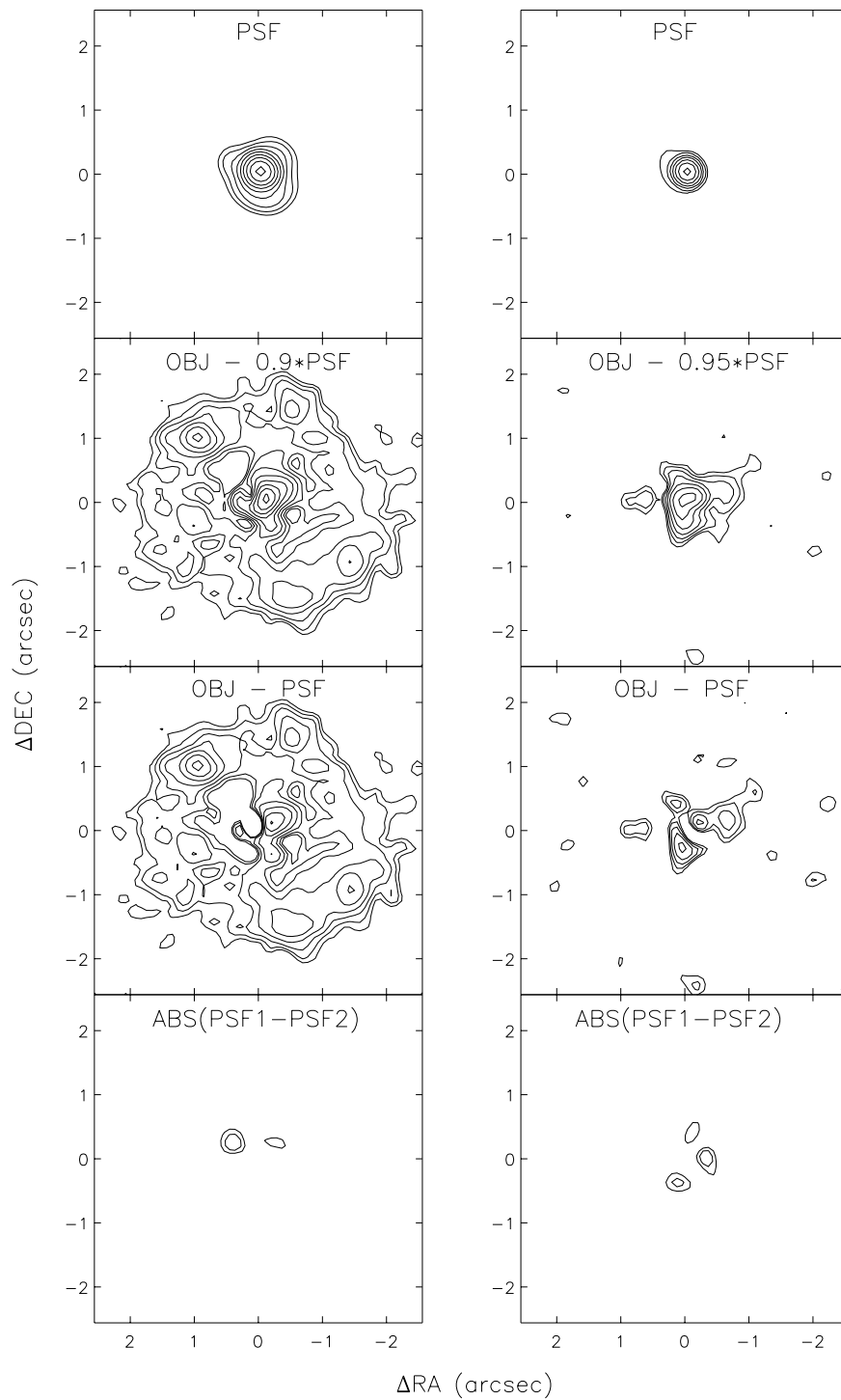
FIG. 3.—Raw PSF is plotted in the top row for NGC 7469 and NGC 1275. The object image minus 0.9 (in the case of NGC 7469) or 0.95 (in the case of NGC 1275) times the PSF is plotted in the second row, and the object minus PSF is plotted in the third from top row. The number of contours is the same in each of the top three rows. PSF residuals obtained by differencing half the PSF images against the other half are plotted in the bottom row. North is up and east to the left. All images are smoothed with a 0″.3 FWHM Gaussian beam to emphasize the extended emission and plotted with contours separated by multiplicative intervals of $\sqrt{2}$. The PSF is normalized to the peak of the object image before subtraction. The PSF residuals are scaled such that the bottom contour, as a fraction of PSF flux, matches the bottom contour plotted in the object minus PSF panel, as a fraction of object flux. The two PSFs images used to generate the PSF residuals image were carefully selected to mimic the matching between the PSF and object. Since the amount of data used to generate the each PSF is halved, we expect that the residuals are overestimated.

(de Vaucouleurs et al. 1991)—implies it is at an inclination angle of ~45°.

The surface luminosity densities of the three compact nuclei, as listed in Table 4, are on the order of a few times 10^{14} $L_{\odot}$ kpc^{-2}. Soifer et al. (2000) found that, of seven ultra-luminous infrared galaxies (ULIRGs) observed in the mid-infrared with the Keck 10 m Telescope, only Markarian 231, a known Seyfert 1 galaxy, has a luminosity density as
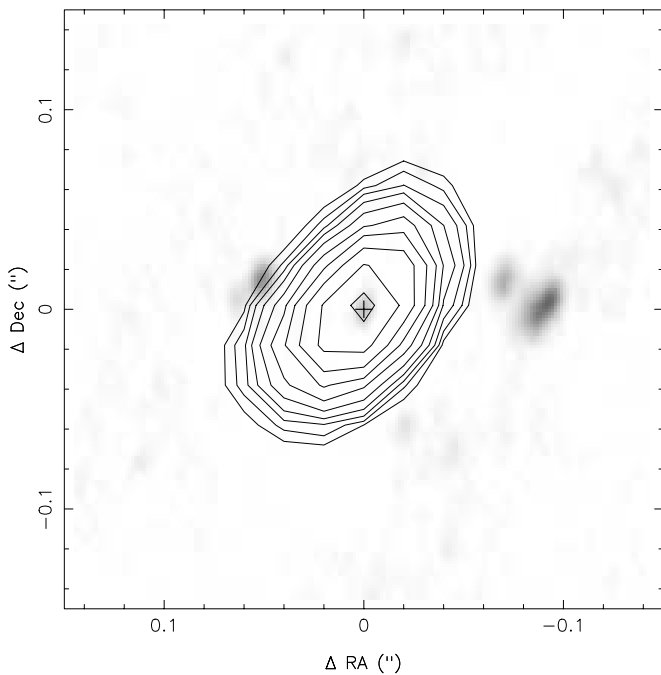
FIG. 4.—Contours of the deconvolved image of NGC 7469 at 12.5 μm, as given in Fig. 2, are overlaid on the VLBI image of Lonsdale et al. (2003). The central source of the VLBI image has been assumed to coincide with the infrared source.

high as 10^{14} $L_\odot$ kpc^{-2}. The difference between starbursts and AGNs is heightened by an examination of the surface brightnesses of infrared luminous galactic nuclei listed by Soifer et al. (2000), Soifer et al. (2001), and Evans et al. (2003). Galactic H II regions have surface brightnesses that range from 2×10^{11} to 2×10^{12} $L_\odot$ kpc^{-2}, those of the starburst galaxies studied range from 2×10^{11} to 10^{13} $L_\odot$ kpc^{-2}, while those of the ULIRGS, with the exception of Markarian 231, range from 2×10^{12} to 6×10^{13} $L_\odot$ kpc^{-2}. Gorjian, Turner, & Beck (2001) have reported the infrared surface brightness of a "super"–star cluster of $\sim 3 \times 10^{14}$ $L_\odot$ kpc^{-2} over 1–2 pc in the nucleus of NGC 5253. While the peak surface brightness in the super–star cluster matches that of the Seyfert galaxies the physical extent of the super–star cluster is smaller, consistent with the 1–2 orders of magnitude lower luminosities compared with the Seyfert nuclei. Thus, it is seen that the infrared surface brightness of those galaxies with evidence of AGN activity is significantly higher than that of those dominated by star formation, and we can conclude that star formation provides only a negligible fraction on the luminosity of the nuclei of the Seyfert galaxies measured here. These results argue that the infrared surface brightness, in concert with the infrared luminosity, can be used as a diagnostic measure for the presence of starbursts or AGNs. These observations can be used to measure the relative contributions of AGN and starbursts to the energy budgets of infrared luminous galaxies provided that the AGN is not heavily obscured at the observed wavelength.

7. SUMMARY

High spatial resolution observations at 12.5 μm were made with the 10 m diameter Keck Telescope in order to study the central nuclei of three Seyfert galaxies.

1. The observations, when deconvolved, resolve a linear structure in the Seyfert galaxy NGC 7469 that is ($<$13) $\times$ 26 pc. The orientation of the infrared emission, when compared with CO and radio observations, supports the conjecture that the mid-infrared emission traces a disk.

2. The observations do not detect structure in the nuclei of NGC 1275 (FWHM $<$ 28 pc) or of NGC 4151 (FWHM $<$ 10 pc). The former limits are within a factor of 2 of being able to resolve a significant contribution to the total emission by thermal emission of centrally heated dust grains.

3. There are indications of underlying extended emission of about 300 pc in NGC 7469 and NGC 1275.

4. The luminosity surface brightness derived for the three Seyfert galaxies are a few times 10^{14} $L_\odot$ kpc^{-2}, significantly higher than that associated with starbursts.

APPENDIX A

PSF STABILITY

The stability of the PSF accompanying NGC 7469 was estimated by deconvolving a synthesized image of the PSF calibrator by a complementary set of independent images of the PSF calibrator. It is important to accurately match the two PSF images in time and air mass. When deconvolving the NGC 7469 image, the average air mass of the object differs only by 0.005 from the average air mass of the PSF, and the average time interval between object and PSF subimages is 8 minutes.

Subgroups to serve as the object and PSF were synthesized using the fact that each of the four subimages of the PSF actually consists of four independent chop-nod sets; in Table A1, these are called a, b, c, and d. The composition of several synthesized PSFs is shown in Table A1. Each pair of PSFs are independent and were chosen with variable matching of the PSF pair in time and air mass. Deconvolved images resulting from the use of one subgroup as PSF and one as object are illustrated in Figure 5. Close matching in time and air mass (e.g., PSF_C/PSF_D) produce pointlike deconvolved images. Poor matching in air mass (e.g., PSF_12/PSF_34) results in significant extensions. Matching in air mass seems to be somewhat more important than matching in time, as the PSF_13/PSF_24 and PSF_12/PSF_34 pairs produce the most extended deconvolved images. For example, the pair PSF_14/PSF_23 has the

<div align="center">SOIFER ET AL.</div>

<div align="center">TABLE A1</div>
<div align="center">SYNTHESIZED PSF IMAGES</div>

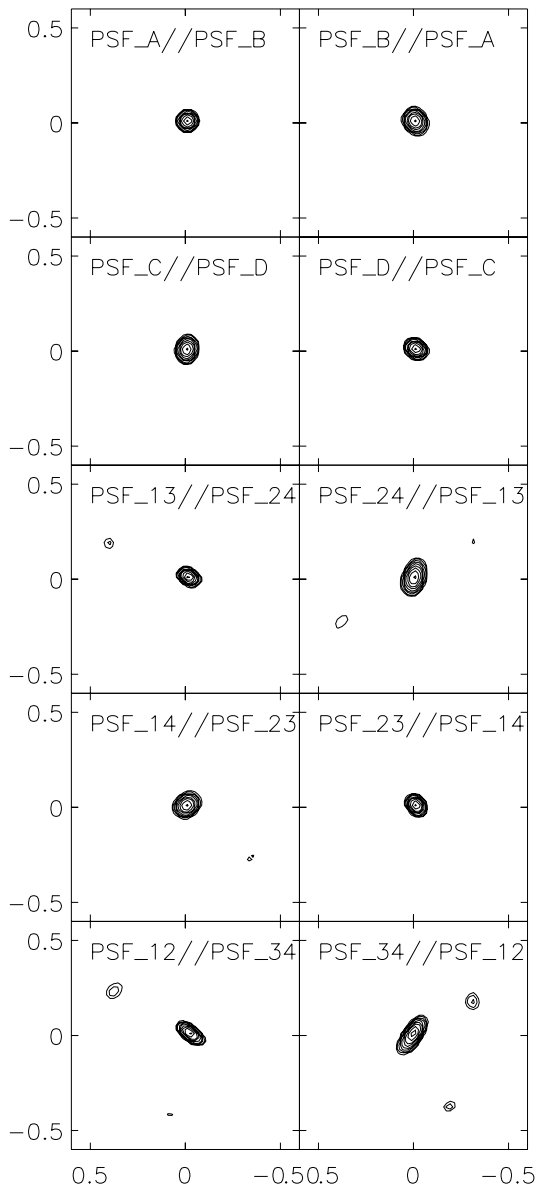| PSF	1				2				3				4				ΔAM	Δt Min
	a	b	c	d	a	b	c	d	a	b	c	d	a	b	c	d		
A.................	X	X			X	X			X	X			X	X			0.000	3
B.................			X	X			X	X			X	X			X	X		
C.................	X				X	X	X			X	X	X				X	0.002	10
D		X	X	X				X	X				X	X	X			
13................	X	X	X	X					X	X	X	X					0.025	18
24................					X	X	X	X					X	X	X	X		
14................	X	X	X	X									X	X	X	X	0.005	30
23................					X	X	X	X	X	X	X	X						
12................	X	X	X	X	X	X	X	X									0.045	30
34................									X	X	X	X	X	X	X	X		

FIG. 5.—Deconvolved images of the PSF accompanying NGC 7469, synthesized as listed in Table A1, are given (see Appendix A). The images are all displayed with contours spaced by multiplicative factors of 2, ranging from 90% of maximum to 0.35% of maximum. North is up, and east is to the left.

same time interval as the pair PSF_12/PSF_34 but much better matching in air mass. The most representative matching for purposes of deconvolving the object are PSF_C/PSF_D.

APPENDIX B

NGC 7469

The image of NGC 7469 was deconvolved by combining all of the object and PSF data. The object and PSF images are very closely matched in air mass and time interval (see Table B1). The data set was divided into independent images of the object and PSF to assess the stability of the northwest-southeast extension in the deconvolved image of NGC 7469. Splitting the data into two independent images of NGC 7469 and the PSF, N_12/PSF_12 and N_34/PSF_34, results in two images that both show a similar northwest-southeast extension (see Fig. 6). This agreement is remarkable given that the image pairs are completely independent. As shown in Figure 6, further subdividing the data into four subimages and PSFs results in four individual images that all show the northwest-southeast extension. Furthermore, all images also show two smaller isolated structures located about 0".5 to the northwest and southwest. A smaller structure located ∼0".3 to the east is seen in the two image pairs, but not in each of the four independent subimages.

APPENDIX C

STATISTICAL SIGNIFICANCE OF THE STRUCTURE

The statistical significance of the elongated structure apparent in the deconvolved images of NGC 7469 was evaluated by comparing the quality of fit of the hypothesized elongated source to that obtained under the assumption of a simple point source. This comparison is based on the residuals with respect to the observed data for the two cases, taking into account our knowledge of the properties of the measurement noise. The residual images are shown in Figures 7e and 7f, along with the sequence of images used to generate them, consisting of the observed image (Fig. 7a), the PSF (Fig. 7b), the " model " image representing the central source obtained by deconvolution (Fig. 7c), and the

OBJECT[a]	1 N	1 P	2 N	2 P	3 N	3 P	4 N	4 P	ΔAM	Δt Min
N_T	X		X		X		X		0.005	8
PSF_T		X		X		X		X		
N_12	X		X						0.005	8
PSF_12		X		X						
N_34					X		X		0.005	8
PSF_34						X		X		
N_1	X								0.000	8
PSF_1		X								
N_2			X						0.010	8
PSF_2				X						
N_3					X				0.000	8
PSF_3						X				
N_4							X		0.010	8
PSF_4								X		

NOTE.—Units of right ascension are hours, minutes, and seconds, and units of declination are degrees, arcminutes, and arcseconds.

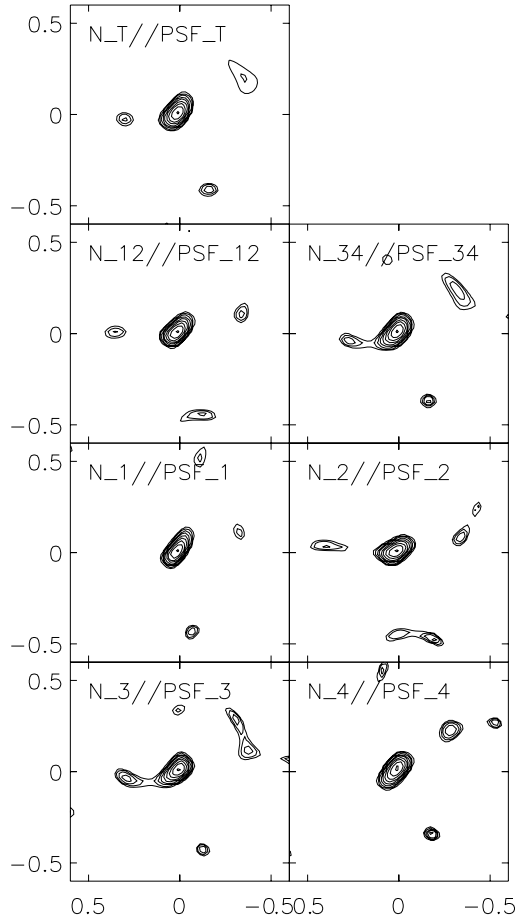[a] (N) NGC 7469; (PSF) PSF star HR 8815.

FIG. 6.—Deconvolved image of NGC 7469 combining all of the data is given in the top image and is compared to independent data subsets in the lower images (see Table B1). Using the first two images of the object and PSF, and the second two images of the object and PSF, result in N_12/PSF_12 and N_34/PSF_34, respectively. These images bear a strong resemblance to the N_T/PSF_T image from the total data set. Further subdivisions of the images into four independent subsets (bottom four images) are also shown. The images are all displayed with contours spaced by multiplicative factors of 2, ranging from 90% of maximum to 0.35% of maximum. North is up and east is to the left.
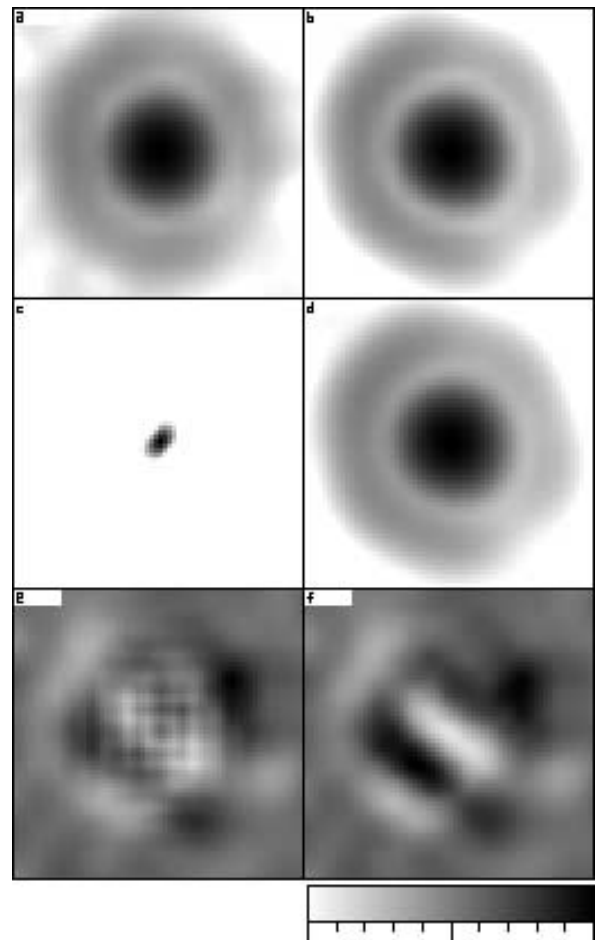

FIG. 7.—(a) Observed (shift and add) image of NGC 7469; (b) PSF image; (c) model image of the extended source (representing the central portion of the deconvolved image); (d) convolution of model image with PSF; (e) residual image, obtained by subtracting (d) from (a); and (f) residual image obtained from the best fit to a point source, for comparison. All images have a field of view of 1″28 × 1″28 and are presented on a sampling grid whose spacing is 0.25 focal plane pixels. The intensity scale is logarithmic (two decades) for (a)–(d) and linear for (e) and (f).

model image convolved with the PSF (Fig. 7d). The residual image Figure 7e was obtained by subtracting Figure 7d from 7a and is to be compared with Figure 7f, which represents the residual image corresponding to the best point-source fit, i.e., the residual image obtained by subtracting Figure 7b from 7a. The comparison of Figures 7e and 7f shows that the residuals are noticeably lower for the extended source than for the point source.

The relative probabilities of the two source-geometry hypotheses can be calculated by comparing the conditional probabilities of the extended source and a point source given the data (represented by a vector $\mathbf{y}$, whose components represent the pixel values of the observed image) by $P(\mathrm{ext}|\mathbf{y})$ and $P(\mathrm{point}|\mathbf{y})$. A simple application of Bayes' rule then yields

$$\ln P(\mathrm{ext}|\mathbf{y})/P(\mathrm{point}|\mathbf{y})$$
$$= \tfrac{1}{2} \sum_i [(y_i - c_i^{\mathrm{point}})^2 - (y_i - c_i^{\mathrm{ext}})^2]/\sigma_i^2 , \quad (C1)$$

where c_i^{point} and c^{ext} represent the point-source and extended-source model images convolved with the PSF, respectively, and σ_i represents the measurement noise in the ith pixel. The summation is over all statistically independent pixels in the image. In deriving this equation, a flat prior was assumed, representing equal a priori probabilities of extended and point sources.

The measurement noise is assumed to be a Gaussian random process with variance:

$$\sigma_i^2 = \sigma_{\mathrm{bg}}^2 + f^2 V_i , \quad (C2)$$

where σ_{bg} is the standard deviation of the background (obtained using pixels far from the source itself), f is the source strength in data units, and V_i is the "variance map" of the PSF, representing the normalized value of PSF uncertainty as a function of position. The PSF variance map was obtained using the deconvolution residuals of four independent subimages of the PSF calibrator and smoothing the result using a 5×5 pixel boxcar averaging window. The PSF uncertainty term in the above expression represents a good approximation in the case of a marginally resolved source.

Based on this procedure, a probability ratio $P(\mathrm{point}|\mathbf{y})/P(\mathrm{ext}|\mathbf{y}) = 1.5 \times 10^{-5}$ was obtained. After normalizing the sum of the two probabilities to unity, this result implies that the probability that the data were produced by a point source was of this same order, which corresponds to a $4.3\,\sigma$ (or greater) deviation of a Gaussian random variable. We can therefore equate the significance of our result to a $4.3\,\sigma$ detection of source elongation.

REFERENCES

Beichman, C. A., Neugebauer, G., Habing, H. J., Clegg, P. E., & Chester, T. J. 1985, Infrared Astronomical Satellite (IRAS) Catalog and Atlases, Explanatory Supplement (Washington, D.C.: GPO)
Bock, J. J., et al. 2000, AJ, 120, 2904
de Vaucouleurs, G., de Vaucouleurs, A., Corwin, H. G., Jr., Buta, R. J., Paturel, G., & Fouqué, P. 1991, Third Reference Catalogue of Bright Galaxies (New York: Springer)
Evans, A. S., et al. 2003, AJ, 125, 2341
Gorjian, V., Turner, J. L., & Beck, S. C. 2001, ApJ, 554, L29
IRAS Point Source Catalog, Version 2. 1989, Joint IRAS Science Team (Washington, D.C.: GPO)
Jones, B., & Puetter, R. C. 1993, Proc. SPIE, 1946, 610
Keel, W. C. 1996, ApJS, 106, 27
Krolik, J. H. 1999, Active Galactic Nuclei: From the Central Black Hole to the Galactic Environment (Princeton: Princeton Univ. Press)
Lonsdale, C. J., Lonsdale, C. J., Smith, H. E., & Diamond, P. J. 2003, submitted
Lucy, L. B. 1974, AJ, 79, 745
Meixner, M., Puchalsky, R., Blitz, L., Wright, M., & Heckman, T. 1990, ApJ, 354, 158
Miles, J. W., Houck, J. R., Hayward, T. L., & Ashby, M. L. N. 1996, ApJ, 465, 191
Neugebauer, G., Graham, J. R., Soifer, B. T., & Matthews, K. 1990, AJ, 99, 1456
Radomski, J. T., Pina, R. K., Packham, C., Telesco, C. M., Buizer, J. M. D., Fisher, R. S., & Robinson, A. 2003, ApJ, 587, 117
Richardson, W. H. 1972, J. Opt. Soc. Am., 62, 55
Sanders, D. B., Phinney, E. S., Neugebauer, G., Soifer, B. T., & Matthews, K. 1989, ApJ, 347, 29
Seyfert, C. K. 1943, ApJ, 97, 28
Soifer, B. T., et al. 2000, AJ, 119, 509
———. 2001, AJ, 122, 1213
Strauss, M. A., Huchra, J. P., Davis, M., Yahil, A., Fisher, K. B., & Tonry, J. 1992, ApJS, 83, 29
Thean, A. H. C., Gillibrand, T. I., Pedlar, A., & Kukula, M. J. 2001, MNRAS, 327, 369
Varosi, F., & Landsman, W. B. 1993, in ASP Conf. Ser. 52, Astronomical Data Analysis Software and Systems II, ed. R. J. Hanisch, R. J. V. Brissenden, & J. Barnes (San Francisco: ASP), 515
Wilson, A. S., Helfer, T. T., Haniff, C. A., & Ward, M. J. 1991, ApJ, 381, 79